

Reciprocity between local moments and collective magnetic excitations in the phase diagram of $\text{BaFe}_2(\text{As}_{1-x}\text{P}_x)_2$

Jonathan Pelliciani^{a,1,2,3} Kenji Ishii,⁴ Yaobo Huang,^{1,5} Marcus Dantz,¹
 Xingye Lu,¹ Paul Olalde Velasco^{b,1} Vladimir N. Strocov,¹ Shigeru
 Kasahara,⁶ Lingyi Xing,⁷ Xiancheng Wang,⁷ Changqing Jin,^{7,8} Yuji
 Matsuda,⁶ Takasada Shibauchi,⁹ Tanmoy Das,¹⁰ and Thorsten Schmitt^{c1}

¹*Swiss Light Source, Photon Science Division,
 Paul Scherrer Institut, CH-5232 Villigen PSI, Switzerland*

²*Department of Physics, Massachusetts Institute of Technology,
 Cambridge, Massachusetts 02139, USA*

³*NSLS-II, Brookhaven National Laboratory, Upton, NY, 11973, USA*

⁴*Synchrotron Radiation Research Center,
 National Institutes for Quantum and Radiological
 Science and Technology, Sayo, Hyogo 679-5148, Japan*

⁵*Beijing National Lab for Condensed Matter Physics, Institute of Physics,
 Chinese Academy of Sciences P. O. Box 603, Beijing 100190, China*

⁶*Department of Physics, Kyoto University, Sakyo-ku, Kyoto 606-8502, Japan*

⁷*Beijing National Lab for Condensed Matter Physics, Institute of Physics,
 Chinese Academy of Sciences, Beijing 100190, China*

⁸*Collaborative Innovation Center for Quantum Matters, Beijing, China*

⁹*Department of Advanced Materials Science,
 University of Tokyo, Kashiwa, Chiba 277-8561, Japan*

¹⁰*Department of Physics, Indian Institute of Science, Bangalore-560012, India*

^a pelliciani@bnl.gov

^b Current address: Diamond Light Source, Harwell Science and Innovation Campus, Didcot, Oxfordshire,
 OX11 0DE, United Kingdom

^c thorsten.schmitt@psi.ch

Abstract

Unconventional superconductivity arises at the border between the strong coupling regime with local magnetic moments and the weak coupling regime with itinerant electrons, and stems from the physics of criticality that dissects the two. Unveiling the nature of the quasiparticles close to quantum criticality is fundamental to understand the phase diagram of quantum materials. Here, using resonant inelastic x-ray scattering (RIXS) and Fe- K_{β} emission spectroscopy (XES), we visualize the coexistence and evolution of local magnetic moments and collective spin excitations across the superconducting dome in isovalently-doped $\text{BaFe}_2(\text{As}_{1-x}\text{P}_x)_2$ ($0.00 \leq x \leq 0.52$). Collective magnetic excitations resolved by RIXS are gradually hardened, whereas XES reveals a strong suppression of the local magnetic moment upon doping. This relationship is captured by an intermediate coupling theory, explicitly accounting for the partially localized and itinerant nature of the electrons in Fe pnictides. Finally, our work identifies a local-itinerant spin fluctuations channel through which the local moments transfer spin excitations to the particle-hole (paramagnons) continuum across the superconducting dome.

INTRODUCTION

It is now well established that unconventional superconductivity (SC) originates from a unique and augmented manifestation of the electronic correlation properties that arises as the system is driven towards a quantum critical region via various tuning parameters such as doping and pressure¹⁻¹¹. On one side of the superconducting dome, the correlation strength is strongly enhanced, leading to diverse quantum many-body effects such as the Mott insulating state, non-Fermi-liquid behaviour, and magnetic orders (see Fig. 1a,b)^{3,4,12-14}. On the other side of the dome, the correlation strength is often substantially suppressed, and the low-energy physics can be described by a more conventional Fermi-liquid theory¹¹. The transition region between these two limits of correlation holds a quantum critical point barely understood. Generally, SC is optimized in this intermediate region where the cooperation of a strongly enhanced non-Fermi-liquid behaviour and the presence of a quantum criticality leads to unconventional and not understood physics¹¹. This generic phase diagram suggests that intertwined electronic and magnetic instabilities, arising from the intermediate correlation strength close to this critical region, induce strong Cooper pairing^{3,4,15}.

The physics which determines the evolution of the spin excitations is crucially dependent on the interaction strength of the electrons compared to their bandwidth. We explain this phenomenon schematically in Fig. 1c-g. The non-interacting density of states (DOS) of electrons (Fig. 1c) is renormalized by the interaction in the two extreme limits as: (i) the bands become sharper in the weak coupling quasiparticle picture (Fig. 1d) and (ii) split into two Mott-like bands characterized by local moments in the strong coupling limit (Fig. 1e). (i) In the weak coupling limit, the low-energy spin excitations (χ_{ii} , see Fig. 1d) are very fragile and mix with the particle-hole continuum, failing to form a localized moment. (ii) In the strong coupling limit, the spin excitations across the Mott-bands (χ_{ll} , see Fig. 1e) feature a gapped behaviour on the order of the onsite energy U without the particle-hole continuum^{13,14}. However, as the correlation strength is tuned to the intermediate coupling region (Fig. 1f), the correlated DOS co-hosts the quasiparticle DOS at low-energy and Mott states at high-energy. In this way a new spin-excitation channel (χ_{il} see Fig. 1g) appears, through which the local moment can now decay to the particle-hole (paramagnon) channels across the magnetic quantum critical point (QCP). Fe pnictides (FePns) can be placed in this intermediate region where the interplay of local and itinerant electronic states leads

to high temperature SC^{1,2,11,15}. An important open question in this context is how local magnetic moments and collective spin excitations are evolving across the superconducting dome in FePns.

FePns have a layered structure that reduces dimensionality and the parent compounds exhibit a spin-density wave with collinear antiferromagnetic (AF) order (see Fig. 1b), which gives way to SC via doping as outlined in Fig. 1a¹⁻¹¹. The origin of the magnetism is poised between being itinerant, as in Cr, and localized, as in cuprates or heavy fermion materials^{1,2,5-11,16} producing an uncommon behaviour which has important consequences for the properties of FePns. Theoretical models proposed that the pairing interaction leading to the superconducting phase is provided by residual AF fluctuations persisting upon doping^{3,4,15}. Yet, owing to the contribution of the AF fluctuations from local and itinerant states, a complex interplay between them arises, which is believed to play a crucial role in shaping the superconducting dome. Thus, the experimental study of magnetism across the phase diagram of high temperature superconductors is of vital importance to provide a solid basis for testing these theories.

Inelastic neutron scattering (INS) is the traditional technique of choice to study magnetism, being able to detect magnetic fluctuations in the full Brillouin zone (BZ)^{8,9}. Recently, Resonant Inelastic X-ray Scattering (RIXS) has emerged as a complementary technique to INS by detecting spin excitations in FePns close to the Γ point as summarized in Refs.¹⁷⁻²². The detection of spin excitations is enabled in RIXS thanks to the spin-orbit coupling of the intermediate state mixing the quantum numbers L and S thereby activating a channel for the detection of magnetic excitations^{23,24}. An important consideration when comparing RIXS with INS is the portion of BZ probed by the two techniques, close to the Γ point in the case of RIXS and at the AF wave-vector for the case of INS. Depending on the case this two positions in momentum space can be equivalent or not. Moreover, it is hard to estimate and compare the absolute weight of magnetic excitations in these two regions of BZ, but it is generally accepted that the intensity at the AF wave-vector is higher than close to the Γ point.

In this article, we use RIXS to systematically unveil the persistence and gradual hardening of the spin excitations in isovalently-doped $\text{BaFe}_2(\text{As}_{1-x}\text{P}_x)_2$ across the phase diagram (see Fig. 1a for a graphical description of the doping levels). Upon doping and without nominally injecting charge carriers, the spectral weight of the spin excitations increases. Our RIXS

measurements are complemented with theory placing the Fe-based superconductors in the intermediate region of correlations and well describing the evolution of the spin excitations with the spin susceptibility (χ_s). Additionally, an investigation of the local fluctuating magnetic moment unravels a decrease of the local moment (μ_{bare}) as a function of doping. This apparent dichotomy implies that there is a transfer of magnetic spectral weight from localized to itinerant as imposed by sum rules relations. We argue that the balance between localized and itinerant states is the key to achieve SC and plays an important role for the physics of criticality in $\text{BaFe}_2(\text{As}_{1-x}\text{P}_x)_2$.

RESULTS

Resonant Inelastic X-Ray Scattering (RIXS)

In Fig. 2, we show a selection of raw RIXS spectra and fitting of the elastic line, fluorescence background, and spin excitations for all the doping levels. The RIXS spectra display a low energy mode ascribed to spin excitations dispersing as a function of in plane momentum transfer ($q_{//}$)¹⁷⁻²¹. The bandwidth, better appreciated at high momentum transfer (top row in Fig. 2), gradually increases with doping along both (H,0) and (H,H) as summarized for the highest q points in Fig. 3. The doping increases the width (damping) of the spin excitations leading to broader dispersing modes at high doping levels. This is expected as the hardening of the spin excitations coupled to electron-hole pair excitations naturally leads to further broadening of the spin excitations²⁵. Our main results are presented in Fig. 4a, where we report the doping dependence of the dispersion of the spin excitations extracted from RIXS experiments as dots with error bars, and overlaid on the calculated dynamical spin susceptibility (χ_s). All the doping levels investigated display dispersive spin excitations as shown in Fig. 2 and 4a and in the Supplementary Figure 6. Upon doping the spin excitations, observed in our RIXS experiments, harden in energy by about 45 meV between the parent (x=0.0) compound and the most doped compound (x=0.52) at (0.44,0). The hardening for the same doping levels at (0.32,0.32) is on the order of 65 meV as summarized in Fig. 3.

The hardening of the spin excitations has been observed by INS for $\text{BaFe}_2(\text{As}_{0.7}\text{P}_{0.3})_2$ ²⁶. At the zone boundary INS observed a hardening of the spin excitations from 180 meV

($x=0$) to 220 meV ($x=0.3$) very similar to what is detected in our RIXS data (180 meV to about 205 meV at $[0.44, 0]$). The small difference between INS and RIXS emerges from slightly different positions in reciprocal space ($[0.5,0]$ vs. $[0.44,0]$) and doping levels ($x=0.3$ vs. $x=0.28$). The comparison to these INS measurements establishes that RIXS probes spin excitations in FePns similarly to INS, even if mixing with other channels such as charge and orbital needs to be considered^{27,28}. The broadening effects as a function of doping detected by our RIXS experiments have been observed by INS as well, where the local susceptibility clearly shows a synergy of hardening and broadening for $x=0.3$.

The persistence of spin excitations along the superconducting dome was previously observed in both electron- and hole-doped FePns but with different effects on the energy of these modes. In hole-doped $\text{Ba}_{1-x}\text{K}_x\text{Fe}_2\text{As}_2$, the spin excitations soften upon doping due to the increase of the electronic correlations as demonstrated by theoretical calculations and accurate measurements of the Sommerfeld constant²⁹⁻³¹. In electron-doped FePns a different behaviour has been detected with the spin excitations being unaffected by doping in their bandwidth but with a decrease of spectral weight^{29,32}. In our present work, we uncover that the energy of the spin excitations increases upon isovalent doping and do not directly correlate with the critical temperature (T_c). This indicates that T_c is likely connected to other microscopic details aside the effective exchange constant. Thus, the case of isovalent $\text{BaFe}_2(\text{As}_{1-x}\text{P}_x)_2$ reveals an unprecedented behaviour, in stark contrast to hole- and electron-doped BaFe_2As_2 , adding new features to the large diversity in the doping effects and magnetism in FePns.

The persistence of spin excitations in unconventional superconductors outside the anti-ferromagnetic parent compound is also a hallmark of the cuprates³³⁻³⁷, where paramagnons have been observed across all the phase diagram. In cuprates, the energy evolution of the spin excitations upon doping is different than the case of FePns: in hole-doped cuprates there is a more or less constancy of the bandwidth along the antinodal direction whereas electron-doped cuprates display hardening of the magnetic excitations³⁵⁻³⁷.

Momentum Resolved Density Fluctuations theory

One approach able to describe the regime of intermediate coupling is Momentum Resolved Density Fluctuations (MRDF) theory. MRDF dissects the electronic spectrum into strongly

renormalized, incoherent ‘local’ states, and low-energy, itinerant Bloch states as displayed in Fig. 1f. The back-reaction of the quantum fluctuations to the electronic states leads to momentum, energy, and orbital dependent renormalization as well as lifetime broadening. Within the quantum field theory, these effects are captured by the real and imaginary part of the self-energy correction³⁸. MRDF theory self-consistently computes the dynamical correlation functions and the corresponding self-energy in the full momentum and energy space^{15,38}. This theory captures the momentum and energy dependent evolution of the localized states as well as the dispersive quasiparticle states, resulting in an anisotropic pairing symmetry, compatible with what is observed experimentally^{3,4}.

To describe the spin excitations probed by RIXS, the dynamical susceptibility (χ) has been calculated and decomposed into the spin (χ_s) and charge (χ_c) channels with both the Random Phase Approximation (RPA) and MRDF method. The intensity of χ_s dominates over χ_c in agreement with a previous work²⁰. Density Functional Theory (DFT)-RPA calculations fail to distribute the spectral weight between the local and itinerant states and overestimate the peak energy of the spin excitations compared to our experimental data (see Supplementary Figs. 10 and 11 and Supplementary Notes 1 and 2). The reason for this is that DFT-RPA underestimates the electronic correlations strength placing the spin excitations at too high energy. Moreover, these RPA calculations cannot account for the hardening of the spin excitations dispersion observed upon doping. In Fig. 1g, we show an idealized scheme of the excitations pattern achieved in the intermediate coupling region comprising local-local (χ_{ll}), local-itinerant (χ_{li}), and itinerant-itinerant excitations (χ_{ii}). The low energy χ_{ii} excitations have an energy in the order of the spin gap ($\approx 1-10$ meV) and are not observable by RIXS due to current limitations of the energy resolution but are observed in INS^{8,9}. The high energy χ_{ll} appears at energies of 900-1500 meV and are not detectable by RIXS due to the intense fluorescence background. The χ_{li} excitations are the (para)-magnon excitations and can be qualitatively compared with our RIXS measurements as a function of doping.

In Fig. 4b,c, we depict the doping dependence of χ_s directly extracted from the MRDF calculations as well as the RIXS spectra at (0.44,0). To better visualize the renormalization in energy of the magnetic excitations we also take the difference between selected doping levels and the parent compound and present the results in Fig. 4d for both theory and experiments. The agreement between theory and experiment is remarkable individuating the

MRDF and more in general the intermediate coupling approach as appropriate to describe the magnetism and electronic structure of FePns. In previous works DFT-RPA has been employed to successfully describe the spin excitations in overdoped cuprates³⁹⁻⁴¹. The failure of DFT-RPA to account for the spin excitations in $\text{BaFe}_2(\text{As}_{1-x}\text{P}_x)_2$ implies that the FePns are not weakly correlated systems and cannot be compared to overdoped cuprates with reduced electronic correlations but rather need to be placed in the family of multiorbital correlated systems similarly to heavy fermion materials^{16,39}.

X-Ray Emission Spectroscopy

To complement our measurements of the spin excitations and assess the local magnetism of $\text{BaFe}_2(\text{As}_{1-x}\text{P}_x)_2$, we employed X-ray Emission Spectroscopy (XES) - a classical technique that has been established as a sensitive probe of the local magnetic moment (μ_{bare})^{19,42-48}. XES is sensitive to the local fluctuating magnetic moment and does not require a net magnetization or ordering, such as X-ray Magnetic Circular Dichroism (XMCD) or neutron diffraction, but detects directly the paramagnetic moment⁴⁴⁻⁴⁶. In this technique, a photon ($h\nu = 7140$ eV) excites an Fe- $1s$ core-electron into the continuum, creating a core-hole which is filled by a Fe- $3p$ electron with the consequent emission of a photon ($h\nu = 7040-7065$ eV). The final Fe- $3p^5$ state has a wave function partly overlapped with the Fe- $3d$ orbitals, and is, thereby, affected by the spin of the valence band through the exchange interaction^{19,42-45,47-49}. The femtosecond timescale of this technique allows for the measurement of fast fluctuations of μ_{bare} ^{5,42,43,49}, and by means of normalization and calibration [carried out with FeCrAs ($0 \mu_B$) and BaFe_2As_2 (set arbitrarily to one to define a relative scale)] μ_{bare} can be determined^{42,43,49}.

In Fig. 5a,b, we show XES spectra for BaFe_2As_2 , and $\text{BaFe}_2(\text{As}_{1-x}\text{P}_x)_2$ ($x=0.52$), and FeCrAs and the respective difference spectra. Clearly, a gradual decrease of μ_{bare} is inferred from the difference spectra depicted in Fig. 5c. The values of μ_{bare} , presented in Fig. 5d,e are continuously reduced, (for example $\mu_{bare} = 1.0 \pm 0.1$ for $x = 0.00$, $\mu_{bare} = 0.6 \pm 0.1$ for $x = 0.28$, and $\mu_{bare} = 0.4 \pm 0.1$ for $x = 0.52$), but not fully quenched by doping, despite the complete disappearance of the ordered magnetic moment observed by neutron scattering^{50,51}. This evidence is remarkable in light of the constancy of the Fe oxidation state observed in XAS (see Supplementary Fig. 2) with isovalent doping driving the antiferromagnetically

long range ordered BaFe_2As_2 into a paramagnetic phase.

We compare the doping dependence of the local moment with the strength of the Fermi surface (FS) nesting at the antiferromagnetic wavevector. In Fig.5**d**, the theoretical data is presented as $\Delta\chi(x) = \chi(x) - \chi(0.6)$, where $\chi(x)$ is the computed static susceptibility at the antiferromagnetic wavevector at doping x [we normalize $\Delta\chi(x=0) = 1$]. Note that this comparison is only qualitative, and a self-consistent estimation of the static magnetic moment is computationally expensive. Similar doping dependence of the magnetic instability arising from the FS nesting and the observed local moment indicates an electronic mechanism of the magnetic ground state in this system.

DISCUSSION

Our XES results are puzzling and assuming spectral weight sum rules, there has to be spectral weight transfer from localized moments into spin excitations as probed by RIXS. In Fig. 5**e**, we report the integrated spectral weight of the spin excitations determined from our RIXS spectra. Within error bars, the spin excitations intensities detected in the portion of BZ pertinent to RIXS possibly show gradual transfer of spectral weight upon doping. However, additional enhancement of spectral weight in different regions of the BZ could be observed. On this aspect, further combined studies of RIXS and high energy INS as a function of doping are required to shed light on the redistribution of spectral weight in the complete BZ. In Fig. 5**e**, we observe the gradual transfer of spectral weight from local magnetic moments into collective spin excitations across the superconducting dome. This spectral redistribution signals that SC is optimized by a balance of these types of interactions.

In summary, we unveiled the persistence and hardening of magnetic excitations along the superconducting dome of $\text{BaFe}_2(\text{As}_{1-x}\text{P}_x)_2$ with concomitant decrease of local magnetic moments. The spectral weight of the spin excitations observed with RIXS slightly increases corroborating that SC emerges from a balance of localized and itinerant electronic interactions. The experimental results agree well with intermediate coupling calculations placing the FePns in the family of multi-orbital correlated systems and uncovering clearly the mixed electronic and magnetic interactions present with optimal superconductivity.

METHODS

Sample preparations

Single crystals of $\text{BaFe}_2(\text{As}_{1-x}\text{P}_x)_2$ were grown either by stoichiometric melt⁵² or $\text{Ba}_2\text{As}_3 / \text{Ba}_2\text{P}_3$ self-flux method⁵³. The samples were characterized either with resistivity or magnetization measurements. For $x = 0.15, 0.22, 0.27,$ and 0.48 , crystals grown by the stoichiometric melt technique were used for the Resonant Inelastic X-ray Scattering (RIXS) experiments, while for $x = 0.38$ and 0.52 we use the crystals grown by the self-flux technique. Supplementary Figure 1 shows the temperature dependence of the resistivity on crystals selected from the same batches. For $x > 0.3$ the Spin Density Wave (SDW) long range order is completely suppressed^{52,53}.

X-ray Absorption Spectroscopy and Resonant Inelastic X-ray Scattering

X-ray Absorption Spectra (XAS) and RIXS experiments were performed at the ADDRESS beamline of the Swiss Light Source, Paul Scherrer Institut, Villigen PSI, Switzerland^{54,55}. In agreement with previous works^{17-20,56}, the samples were mounted with the ab plane perpendicular to the scattering plane and the c axis lying in it (sketch in Supplementary Figure 2) and post-cleaved *in-situ* at a pressure better than 2.0×10^{-10} mbar. The reciprocal space directions studied are $(0, 0) \rightarrow (1, 0)$ and $(0, 0) \rightarrow (1, 1)$ according to the orthorhombic unfolded crystallographic notation. The values of in-plane momentum transferred are expressed as relative lattice units (RLU) ($q_{//}a / 2\pi$). We use the convention of 1 Fe per unit cell. All the measurements were carried out at 13 K by cooling the manipulator with liquid helium. XAS spectra were measured in both Total Fluorescence Yield (TFY) and Total Electron Yield (TEY) modes. No difference was observed between TEY and TFY which indicates the sample integrity across the thickness probed in our experiment. We measured Fe $L_{2,3}$ XAS spectra for all samples at 15 degrees of incidence angle relative to the sample surface. All the XAS spectra are reported in Supplementary Figure 3 and display the constancy of the iron oxidation state. There are small spectral differences at around 710 eV that are possibly due to a different covalency between the FeAs and FeP.

The RIXS spectrometer was set to a scattering angle of 130 degrees and the incidence angle on the samples surface was varied to change the in-plane momentum transferred ($q_{//}$)

from (0, 0) to (0.44, 0) and from (0, 0) to (0.31, 0.31). All RIXS measurements in the present paper were recorded in grazing incidence configuration as depicted in Supplementary Figure 2. The zero energy loss of our RIXS spectra was determined by measuring spectra in σ polarization. The total energy resolution was measured employing the elastic scattering of carbon-filled acrylic tape and is around 110 meV.

RIXS spectra were normalized to unity and the main emission line was fitted according to Ref.^{17-20,56} employing the following formulas:

$$I_{fit} = (\beta x^2 + \alpha x + c) \cdot (1 - g_\gamma) + I_0 \exp(ax) \cdot g_\gamma + G \quad (1)$$

with

$$g_\gamma = \left(\exp\left(\frac{x + \omega^*}{\Gamma}\right) + 1 \right)^{-1} \quad (2)$$

and

$$G = \frac{A}{\sigma\sqrt{2\pi}} \exp\left(-\frac{(x + x_0)^2}{2\sigma^2}\right) \quad (3)$$

In the first formula, the first part is a 2^{nd} order polynomial function describing the emission line at low energy loss, the second part is an exponential decay describing the emission line at high energy loss. The two behaviours are swapped into each other by the g_γ term. The third term is a gaussian curve (G) observed at around -4.2 eV energy loss. An exemplary fitting of the full RIXS spectra is drawn in Supplementary Figure 4 for BaFe₂As₂ at (0.44, 0.0).

In Supplementary Figure 5, we show RIXS spectra over an extended range of energy loss. Overall, the three spectra resemble a metallic system with the lineshape not being affected by doping. Due to changes in the band structure upon doping, small energy shifts and changes in the RIXS intensity are detected.

We complemented the momentum dependence along (0, 0)→(1, 0) with (0, 0)→(1, 1) and display the raw data for all the dopings and momenta with the fitting in Supplementary Figure 6.

K_{β} Emission Spectroscopy

We performed the Fe- K_{β} x-ray emission (XES) experiments at BL11XU of SPring-8, Japan. The incoming beam was monochromatized by a Si (111) double-crystal and a Si (400) secondary channel-cut crystal. The energy was calibrated by measuring x-ray absorption of a Fe foil and set to 7.140 keV with π polarization. We employed three spherical diced Ge (620) analyzers and a detector in Rowland geometry at 2 m distance. The total combined resolution was about 400 meV estimated from Full Width Half Maximum (FWHM) of the elastic line. We scanned the absolute emission energy between 7.02 keV and 7.08 keV and normalized the intensity by the incident flux monitored by an ionization chamber. We carried out the measurements at 15 K. The experimental geometry of the experiment is depicted in Supplementary Figure 7. The determination of μ_{bare} were performed employing the integrated absolute difference (IAD) method described by Vanko' et al.⁴⁵. The areas of the XES spectra were normalized to unity as shown in Supplementary Figure 8a-f. To overcome problems of alignment of the absolute energy between different samples, we estimated the center of mass of the spectra and aligned the energy to have the same center of mass as described by Glatzel et al.⁴⁴. Then the difference with the spectrum of the FeCrAs reference was taken as displayed in Supplementary Figure 8a-f and summarized in Supplementary Figure 8g. The integration of this difference gives the IAD, which is directly proportional to μ_{bare} ⁴⁵.

Doping dependent band structure

Two extreme doping regimes of the $\text{BaFe}_2(\text{As}_{1-x}\text{P}_x)_2$ samples, namely BaFe_2As_2 ($x = 0.00$) and BaFe_2P_2 ($x = 1.00$) have been studied within density functional theory (DFT)⁵⁷. Also accurate tight-binding models are available to reproduce the DFT band structure, consistent with Angle Resolved Photoemission Spectroscopy (ARPES) data (after including renormalization effects). However, P-doping effects on the As site, which does not change the carrier concentration, is neither trivial to accurately calculate within the DFT framework, nor within a simple rigid band shift technique which works reasonably well for electron and hole doping cases⁵⁸. Since P atom is smaller in size compared to As atoms, P doping is expected to decrease the lattice volume. Indeed, both x-ray⁵², and neutron⁵¹ diffraction

analysis revealed that all three lattice constants as well as the pnictogen atomic coordinates in the unit cell (z_{Pn}) and the pnictogen height from the Fe plane (h_{Pn}) decrease monotonically with P doping. Among them, the c -axis lattice constant decreases drastically from ≈ 13 Å at $x = 0.00$ to ≈ 12.4 Å at $x = 1.00$. This explains why the three-dimensionality of the sample (i.e. k_z dispersion) increases considerably with doping, as consistently demonstrated in both ARPES⁵⁹ as well as in de Haas-van Alphen measurements^{60,61}. It is shown that throughout the entire doping range, the Fermi surface (FS) topology remains very similar and consists of hole pockets at the Γ -point and electron pockets at the M-point. At $x = 0.00$, there are three concentric hole pockets, which reduce to only two remaining hole pockets at $x = 1.00$, with the smaller pocket disappearing at some intermediate doping. The electron-like FS consists of two elliptic electron pockets interpenetrating to each other¹¹. Among all the FS pockets, the outermost hole-pocket shows most dominant and drastic changes with doping: It is very close to cylindrical as a function of k_z at $x = 0.00$, but gradually becomes corrugated with increasing doping. The other pockets acquire comparatively less k_z dispersion⁵⁹⁻⁶¹. This could be quantified by calculating the nesting strength via the integration of the static susceptibility at the nesting wave-vector. The nesting strength has been shown to decrease upon doping^{11,58,60}. Projected orbital symmetries on each FS reveal that the hole pockets are dominated by the d_{xz} / d_{yz} orbitals, while the electron pockets are made of hybridization between the d_{xz} / d_{yz} orbitals with the d_{xy} orbitals. The d_{z^2} orbital has little contribution at $x = 0.00$, while it grows with doping. d_{z^2} basically contributes to the strongly k_z dispersive parts of the outermost hole-pocket⁶⁰.

Based on the aforementioned experimental observations on the band structure evolution with doping, we construct an effective five-orbital tight-binding (TB) model to reproduce the low-energy dispersion and FS topology across the entire phase diagram. The 2 Fe unit cell incorporates two Fe sublattices producing a 10 band model. We start with a five orbital TB model as derived in Ref.⁵⁷ for BaFe₂As₂. The intra-orbital dispersions are defined by $\xi_k^i = \epsilon_k^i + \Delta^i - \epsilon_F$, where k is the crystal momentum and $i = 1 - 5$ is the orbital index. ϵ_k^i is the momentum dependent part of the dispersion which arises from the nearest, next, and higher neighbour hoppings between the same orbitals, Δ^i is the corresponding on-site potentials, and ϵ_F is the chemical potential. As the unit cell volume decreases monotonically with P doping, it is expected that the electron hopping amplitude increases monotonically with doping. We model this effect by a simple renormalization factor λ as $\epsilon_k^i \rightarrow \lambda \epsilon_k^i$, where λ

increases with doping. Similarly, due to the monotonic increase of the pnictogen coordinate and the height (z_{Pn} , h_{Pn}), the on-site potential also changes. Interestingly, we find that an orbital dependent modification of the on-site potential is required to properly reproduce the experimental behaviour of the k_z dispersion and FS changes. We set $\Delta^i \rightarrow \Delta^i + \delta$ for d_{xz} / d_{yz} orbitals, $\Delta^i \rightarrow \Delta^i - \delta$ for $d_{x^2-y^2}$ and d_z^2 orbitals, $\Delta^i \rightarrow \Delta^i - 2\delta$ for d_{xy} orbital, where $\delta(x) = 0.08x$, with x being the doping value. The chemical potential is adjusted at each doping to keep the same number of electrons. Such a model was also invoked earlier to model the FS topological transition in KFe_2Se_2 under pressure⁶². The corresponding FS topologies at three representative dopings are shown in Supplementary Figure 9.

AUTHORS CONTRIBUTION

Th. Sc. conceived the project. J. P., K.I., Y.H., and Th. Sc. conducted XES experiments. J. P., Y. H., M. D., P. O. V., X. L., and Th. Sc. performed RIXS experiments with the assistance of V. N. S., S. K., Y. M., and Ta. Sh. prepared and characterized P-doped BaFe_2As_2 . L. X., X. W., and C. J. prepared the reference sample for XES. T. D. performed the calculations. J. P., K. I., T.D., and Th. Sc. together planned the project phases. J. P., T.D., and Th. Sc. wrote the manuscript with input from all the authors.

ACKNOWLEDGEMENTS

J.P. and T.S. acknowledge financial support through the Dysenos AG by Kabelwerke Brugg AG Holding, Fachhochschule Nordwestschweiz, and the Paul Scherrer Institut. J. P. also acknowledges financial support by the Swiss National Science Foundation Early Postdoc Mobility fellowship project number P2FRP2_171824 and PostDoc Mobility project number P400P2_180744. We acknowledge Y. Shimizu for the support during the experiments at SPring-8 and D. Casa for fabrication of the Ge (620) analyzers. The Fe- K_β emission experiments were performed at BL11XU of SPring-8 with the approval of the Japan Synchrotron Radiation Research Institute (JASRI) (Proposals No. 2014A3502 and 2014B3502). RIXS experiments have been performed at the ADDRESS beamline of the Swiss Light Source at Paul Scherrer Institut. Part of this research has been funded by the Swiss National Science Foundation through the Sinergia network Mott Physics Beyond the Heisenberg (MPBH)

model (SNSF Research grants numbers CRSII2_141962 and CRSII2_1607651) and the D-A-CH program (SNSF Research Grant No. 200021L_141325). The research leading to these results has received funding from the European Community's Seventh Framework Programme (FP7/2007-2013) under Grant Agreement No. 290605 (COFUND: PSIFEL-LOW). Work in Japan was supported by Grant-in-Aids for Scientific Research (KAKENHI) from Japan Society for the Promotion of Science (JSPS), and by the 'Topological Material Science' Grant-in-Aid for Scientific Research on Innovative Areas from the Ministry of Education, Culture, Sports, Science and Technology (MEXT) of Japan. The work at IOP-CAS is supported by NSF and MOST through research projects.

COMPETING INTERESTS

The authors declare no competing interests.

DATA AVAILABILITY

Data that support the findings of this study are available upon reasonable request from the corresponding authors.

REFERENCES

- ¹ Johnston, D. C. The puzzle of high temperature superconductivity in layered iron pnictides and chalcogenides. *Advances in Physics* **59**, 803–1061 (2010). URL <http://dx.doi.org/10.1080/00018732.2010.513480>.
- ² Stewart, G. R. Superconductivity in iron compounds. *Reviews of Modern Physics* **83**, 1589–1652 (2011). URL <http://link.aps.org/doi/10.1103/RevModPhys.83.1589>.
- ³ Chubukov, A. Pairing Mechanism in Fe-Based Superconductors. *Annual Review of Condensed Matter Physics* **3**, 57–92 (2012). URL <http://dx.doi.org/10.1146/annurev-conmatphys-020911-125055>.
- ⁴ Scalapino, D. J. A common thread: The pairing interaction for unconventional superconductors. *Reviews of Modern Physics* **84**, 1383–1417 (2012). URL <http://link.aps.org/doi/10.1103/RevModPhys.84.1383>.

- ⁵ Mannella, N. The magnetic moment enigma in Fe-based high temperature superconductors. *Journal of Physics: Condensed Matter* **26**, 473202 (2014). URL <http://stacks.iop.org/0953-8984/26/i=47/a=473202>.
- ⁶ Inosov, D. S. Spin fluctuations in iron pnictides and chalcogenides: From antiferromagnetism to superconductivity. *Comptes Rendus Physique* **17**, 60 (2016). URL <http://www.sciencedirect.com/science/article/pii/S1631070515000523>.
- ⁷ Tranquada, J. M., Xu, G. & Zaliznyak, I. A. Superconductivity, antiferromagnetism, and neutron scattering. *Journal of Magnetism and Magnetic Materials* **350**, 148–160 (2014). URL <http://www.sciencedirect.com/science/article/pii/S0304885313006884>.
- ⁸ Dai, P. Antiferromagnetic order and spin dynamics in iron-based superconductors. *Reviews of Modern Physics* **87**, 855–896 (2015). URL <http://link.aps.org/doi/10.1103/RevModPhys.87.855>.
- ⁹ Dai, P., Hu, J. & Dagotto, E. Magnetism and its microscopic origin in iron-based high-temperature superconductors. *Nature Physics* **8**, 709–718 (2012). URL <http://www.nature.com/nphys/journal/v8/n10/abs/nphys2438.html>.
- ¹⁰ Lumsden, M. D. & Christianson, A. D. Magnetism in Fe-based superconductors. *Journal of Physics: Condensed Matter* **22**, 203203 (2010). URL <http://stacks.iop.org/0953-8984/22/i=20/a=203203>.
- ¹¹ Shibauchi, T., Carrington, A. & Matsuda, Y. A Quantum Critical Point Lying Beneath the Superconducting Dome in Iron Pnictides. *Annual Review of Condensed Matter Physics* **5**, 113–135 (2014). URL <http://dx.doi.org/10.1146/annurev-conmatphys-031113-133921>.
- ¹² Lee, P. A., Nagaosa, N. & Wen, X.-G. Doping a Mott insulator: Physics of high-temperature superconductivity. *Reviews of Modern Physics* **78**, 17–85 (2006). URL <http://link.aps.org/doi/10.1103/RevModPhys.78.17>.
- ¹³ Yin, Z. P., Haule, K. & Kotliar, G. Kinetic frustration and the nature of the magnetic and paramagnetic states in iron pnictides and iron chalcogenides. *Nature Materials* **10**, 932–935 (2011). URL <http://www.nature.com/nmat/journal/v10/n12/full/nmat3120.html>.
- ¹⁴ de Medici, L., Hassan, S. R., Capone, M. & Dai, X. Orbital-Selective Mott Transition out of Band Degeneracy Lifting. *Physical Review Letters* **102**, 126401 (2009). URL <https://link.aps.org/doi/10.1103/PhysRevLett.102.126401>.

- ¹⁵ Chubukov, A. V. Itinerant electron scenario for Fe-based superconductors. *Springer Series in Materials Science* **211**, 255–329 (2015). URL <http://xxx.tau.ac.il/abs/1507.03856>.
- ¹⁶ Yang, W. L. *et al.* Evidence for weak electronic correlations in iron pnictides. *Physical Review B* **80**, 014508 (2009). URL <http://link.aps.org/doi/10.1103/PhysRevB.80.014508>.
- ¹⁷ Zhou, K.-J. *et al.* Persistent high-energy spin excitations in iron-pnictide superconductors. *Nature Communications* **4**, 1470 (2013). URL <http://www.nature.com/ncomms/journal/v4/n2/full/ncomms2428.html>.
- ¹⁸ Pellicciari, J. *et al.* Presence of magnetic excitations in SmFeAsO. *Applied Physics Letters* **109**, 122601 (2016). URL <http://scitation.aip.org/content/aip/journal/apl/109/12/10.1063/1.4962966>.
- ¹⁹ Pellicciari, J. *et al.* Local and collective magnetism of EuFe₂As₂. *Physical Review B* **95**, 115152 (2017). URL <https://link.aps.org/doi/10.1103/PhysRevB.95.115152>.
- ²⁰ Pellicciari, J. *et al.* Intralayer doping effects on the high-energy magnetic correlations in NaFeAs. *Physical Review B* **93**, 134515 (2016). URL <http://link.aps.org/doi/10.1103/PhysRevB.93.134515>.
- ²¹ Rahn, M. C. *et al.* Paramagnon dispersion in β -FeSe observed by Fe L-edge resonant inelastic x-ray scattering. *Physical Review B* **99**, 014505 (2019). URL <https://link.aps.org/doi/10.1103/PhysRevB.99.014505>.
- ²² Garcia, F. A. *et al.* Anisotropic magnetic excitations and incipient Neel order in Ba(Fe_{1-x}Mn_x)₂As₂. *Physical Review B* **99**, 115118 (2019). URL <https://link.aps.org/doi/10.1103/PhysRevB.99.115118>.
- ²³ Ament, L. J. P., van Veenendaal, M., Devereaux, T. P., Hill, J. P. & van den Brink, J. Resonant inelastic x-ray scattering studies of elementary excitations. *Reviews of Modern Physics* **83**, 705–767 (2011). URL <http://link.aps.org/doi/10.1103/RevModPhys.83.705>.
- ²⁴ Jia, C., Wohlfeld, K., Wang, Y., Moritz, B. & Devereaux, T. P. Using RIXS to Uncover Elementary Charge and Spin Excitations. *Physical Review X* **6**, 021020 (2016). URL <http://link.aps.org/doi/10.1103/PhysRevX.6.021020>.
- ²⁵ Tohyama, T., Tsutsui, K., Mori, M., Sota, S. & Yunoki, S. Enhanced charge excitations in electron-doped cuprates by resonant inelastic x-ray scattering. *Physical Review B* **92**, 014515 (2015). URL <https://link.aps.org/doi/10.1103/PhysRevB.92.014515>.

- ²⁶ Hu, D. *et al.* Spin excitations in optimally P-doped $\text{BaFe}_2(\text{As}_{1-x}\text{P}_x)_2$ superconductor. *Physical Review B* **94**, 094504 (2016). URL <http://link.aps.org/doi/10.1103/PhysRevB.94.094504>.
- ²⁷ Nomura, T. *et al.* Resonant inelastic x-ray scattering study of entangled spin-orbital excitations in superconducting $\text{PrFeAsO}_{0.7}$. *Physical Review B* **94**, 035134 (2016). URL <http://link.aps.org/doi/10.1103/PhysRevB.94.035134>.
- ²⁸ Kaneshita, E., Tsutsui, K. & Tohyama, T. Spin and orbital characters of excitations in iron arsenide superconductors revealed by simulated resonant inelastic x-ray scattering. *Physical Review B* **84**, 020511 (2011). URL <http://link.aps.org/doi/10.1103/PhysRevB.84.020511>.
- ²⁹ Wang, M. *et al.* Doping dependence of spin excitations and its correlations with high-temperature superconductivity in iron pnictides. *Nature Communications* **4** (2013). URL <http://www.nature.com/ncomms/2013/131204/ncomms3874/full/ncomms3874.html>.
- ³⁰ Eilers, F. *et al.* Strain-Driven Approach to Quantum Criticality in AFe_2As_2 with $\text{A}=\text{K}$, Rb , and Cs . *Physical Review Letters* **116**, 237003 (2016). URL <https://link.aps.org/doi/10.1103/PhysRevLett.116.237003>.
- ³¹ Charnukha, A. *et al.* Intrinsic Charge Dynamics in High- T_c $\text{AFeAs}(\text{O},\text{F})$ Superconductors. *Physical Review Letters* **120**, 087001 (2018). URL <https://link.aps.org/doi/10.1103/PhysRevLett.120.087001>.
- ³² Luo, H. *et al.* Electron doping evolution of the magnetic excitations in $\text{BaFe}_{2-x}\text{Ni}_x\text{As}_2$. *Physical Review B* **88**, 144516 (2013). URL <http://link.aps.org/doi/10.1103/PhysRevB.88.144516>.
- ³³ Dean, M. P. M. *et al.* Persistence of magnetic excitations in $\text{La}_{2-x}\text{Sr}_x\text{CuO}_4$ from the undoped insulator to the heavily overdoped non-superconducting metal. *Nature Materials* **12**, 1019–1023 (2013). URL <http://www.nature.com/nmat/journal/v12/n11/abs/nmat3723.html>.
- ³⁴ Le Tacon, M. *et al.* Intense paramagnon excitations in a large family of high-temperature superconductors. *Nature Physics* **7**, 725–730 (2011). URL <http://www.nature.com/nphys/journal/v7/n9/full/nphys2041.html>.
- ³⁵ Lee, W. S. *et al.* Asymmetry of collective excitations in electron- and hole-doped cuprate superconductors. *Nature Physics* **10**, 883–889 (2014). URL <http://www.nature.com/nphys/journal/v10/n11/abs/nphys3117.html>.

- ³⁶ Ishii, K. *et al.* High-energy spin and charge excitations in electron-doped copper oxide superconductors. *Nature Communications* **5** (2014). URL <http://www.nature.com/ncomms/2014/140425/ncomms4714/abs/ncomms4714.html>.
- ³⁷ Dellea, G. *et al.* Spin and charge excitations in artificial hole- and electron-doped infinite layer cuprate superconductors. *Physical Review B* **96**, 115117 (2017). URL <https://link.aps.org/doi/10.1103/PhysRevB.96.115117>.
- ³⁸ Das, T., Markiewicz, R. S. & Bansil, A. Intermediate coupling model of the cuprates. *Advances in Physics* **63**, 151–266 (2014). URL <http://dx.doi.org/10.1080/00018732.2014.940227>.
- ³⁹ Monney, C. *et al.* Resonant inelastic x-ray scattering study of the spin and charge excitations in the overdoped superconductor $\text{La}_{1.77}\text{Sr}_{0.23}\text{CuO}_4$. *Physical Review B* **93**, 075103 (2016). URL <http://link.aps.org/doi/10.1103/PhysRevB.93.075103>.
- ⁴⁰ Guarise, M. *et al.* Anisotropic softening of magnetic excitations along the nodal direction in superconducting cuprates. *Nature Communications* **5** (2014). URL <http://www.nature.com/ncomms/2014/141218/ncomms6760/abs/ncomms6760.html>.
- ⁴¹ Dean, M. P. M. *et al.* Itinerant effects and enhanced magnetic interactions in Bi-based multilayer cuprates. *Physical Review B* **90**, 220506 (2014). URL <http://link.aps.org/doi/10.1103/PhysRevB.90.220506>.
- ⁴² Gretarsson, H. *et al.* Spin-State Transition in the Fe Pnictides. *Physical Review Letters* **110**, 047003 (2013). URL <http://link.aps.org/doi/10.1103/PhysRevLett.110.047003>.
- ⁴³ Gretarsson, H. *et al.* Revealing the dual nature of magnetism in iron pnictides and iron chalcogenides using x-ray emission spectroscopy. *Physical Review B* **84**, 100509 (2011). URL <http://link.aps.org/doi/10.1103/PhysRevB.84.100509>.
- ⁴⁴ Glatzel, P. & Bergmann, U. High resolution 1s core hole X-ray spectroscopy in 3d transition metal complexes: electronic and structural information. *Coordination Chemistry Reviews* **249**, 65–95 (2005). URL <http://www.sciencedirect.com/science/article/pii/S0010854504001146>.
- ⁴⁵ Vanko, G. *et al.* Probing the 3d Spin Momentum with X-ray Emission Spectroscopy: The Case of Molecular-Spin Transitions. *The Journal of Physical Chemistry B* **110**, 11647–11653 (2006). URL <http://dx.doi.org/10.1021/jp0615961>.
- ⁴⁶ Yamamoto, Y. *et al.* Origin of Pressure-induced Superconducting Phase in $\text{K}_x\text{Fe}_{2-y}\text{Se}_2$ studied by Synchrotron X-ray Diffraction and Spectroscopy. *Scientific Reports* **6**, 30946 (2016). URL

<http://www.nature.com/srep/2016/160808/srep30946/full/srep30946.html>.

- ⁴⁷ Lafuerza, S. *et al.* Evidence of Mott physics in iron pnictides from x-ray spectroscopy. *Physical Review B* **96**, 045133 (2017). URL <https://link.aps.org/doi/10.1103/PhysRevB.96.045133>.
- ⁴⁸ Pellicciari, J. *et al.* Magnetic moment evolution and spin freezing in doped BaFe₂As₂. *Scientific Reports* **7**, 8003 (2017). URL <https://www.nature.com/articles/s41598-017-07286-6>.
- ⁴⁹ Vilmercati, P. *et al.* Itinerant electrons, local moments, and magnetic correlations in the pnictide superconductors CeFeAsO_{1-x}F_x and Sr(Fe_{1-x}Co_x)₂As₂. *Physical Review B* **85**, 220503 (2012). URL <http://link.aps.org/doi/10.1103/PhysRevB.85.220503>.
- ⁵⁰ Hu, D. *et al.* Structural and Magnetic Phase Transitions near Optimal Superconductivity in BaFe₂(As_{1-x}P_x)₂. *Physical Review Letters* **114**, 157002 (2015). URL <http://link.aps.org/doi/10.1103/PhysRevLett.114.157002>.
- ⁵¹ Allred, J. M. *et al.* Coincident structural and magnetic order in BaFe₂(As_{1-x}P_x)₂ revealed by high-resolution neutron diffraction. *Physical Review B* **90**, 104513 (2014). URL <http://link.aps.org/doi/10.1103/PhysRevB.90.104513>.
- ⁵² Kasahara, S. *et al.* Evolution from non-Fermi- to Fermi-liquid transport via isovalent doping in BaFe₂(As_{1-x}P_x)₂ superconductors. *Physical Review B* **81**, 184519 (2010). URL <http://link.aps.org/doi/10.1103/PhysRevB.81.184519>.
- ⁵³ Nakajima, M. *et al.* Growth of BaFe₂(As_{1-x}P_x)₂ Single Crystals (0 ≤ x ≤ 1) by Ba₂As₃/Ba₂P₃-Flux Method. *Journal of the Physical Society of Japan* **81**, 104710 (2012). URL <http://journals.jps.jp/doi/abs/10.1143/JPSJ.81.104710>.
- ⁵⁴ Strocov, V. N. *et al.* High-resolution soft X-ray beamline ADRESS at the Swiss Light Source for resonant inelastic X-ray scattering and angle-resolved photoelectron spectroscopies. *Journal of Synchrotron Radiation* **17**, 631–643 (2010). URL <http://www.ncbi.nlm.nih.gov/pmc/articles/PMC2927903/>.
- ⁵⁵ Ghiringhelli, G. *et al.* SAXES, a high resolution spectrometer for resonant x-ray emission in the 4001600 eV energy range. *Review of Scientific Instruments* **77**, 113108 (2006). URL <http://scitation.aip.org/content/aip/journal/rsi/77/11/10.1063/1.2372731>.
- ⁵⁶ Hancock, J. N. *et al.* Evidence for core-hole-mediated inelastic x-ray scattering from metallic Fe_{1.087}Te. *Physical Review B* **82**, 020513 (2010). URL <http://link.aps.org/doi/10.1103/PhysRevB.82.020513>.

- ⁵⁷ Graser, S., Maier, T. A., Hirschfeld, P. J. & Scalapino, D. J. Near-degeneracy of several pairing channels in multiorbital models for the Fe pnictides. *New Journal of Physics* **11**, 025016 (2009). URL <http://stacks.iop.org/1367-2630/11/i=2/a=025016?key=crossref.a72831a9942b2bd8efb605fbd013abf2>.
- ⁵⁸ Richard, P., Sato, T., Nakayama, K., Takahashi, T. & Ding, H. Fe-based superconductors: an angle-resolved photoemission spectroscopy perspective. *Reports on Progress in Physics* **74**, 124512 (2011). URL <http://stacks.iop.org/0034-4885/74/i=12/a=124512>.
- ⁵⁹ Yoshida, T. *et al.* Two-Dimensional and Three-Dimensional Fermi Surfaces of Superconducting $\text{BaFe}_2(\text{As}_{1-x}\text{P}_x)_2$ and Their Nesting Properties Revealed by Angle-Resolved Photoemission Spectroscopy. *Physical Review Letters* **106**, 117001 (2011). URL <http://link.aps.org/doi/10.1103/PhysRevLett.106.117001>.
- ⁶⁰ Arnold, B. J. *et al.* Nesting of electron and hole Fermi surfaces in nonsuperconducting $\text{BaFe}_{1-x}\text{P}_x$. *Physical Review B* **83**, 220504 (2011). URL <http://link.aps.org/doi/10.1103/PhysRevB.83.220504>.
- ⁶¹ Analytis, J. G., Chu, J.-H., McDonald, R. D., Riggs, S. C. & Fisher, I. R. Enhanced Fermi-Surface Nesting in Superconducting $\text{BaFe}_2(\text{As}_{1-x}\text{P}_x)_2$ Revealed by the de Haas-van Alphen Effect. *Physical Review Letters* **105**, 207004 (2010). URL <http://link.aps.org/doi/10.1103/PhysRevLett.105.207004>.
- ⁶² Das, T. & Balatsky, A. V. Origin of pressure induced second superconducting dome in $\text{A}_y\text{Fe}_{2-x}\text{Se}_2$ [A = K, (Tl,Rb)]. *New Journal of Physics* **15**, 093045 (2013). URL <http://stacks.iop.org/1367-2630/15/i=9/a=093045>.

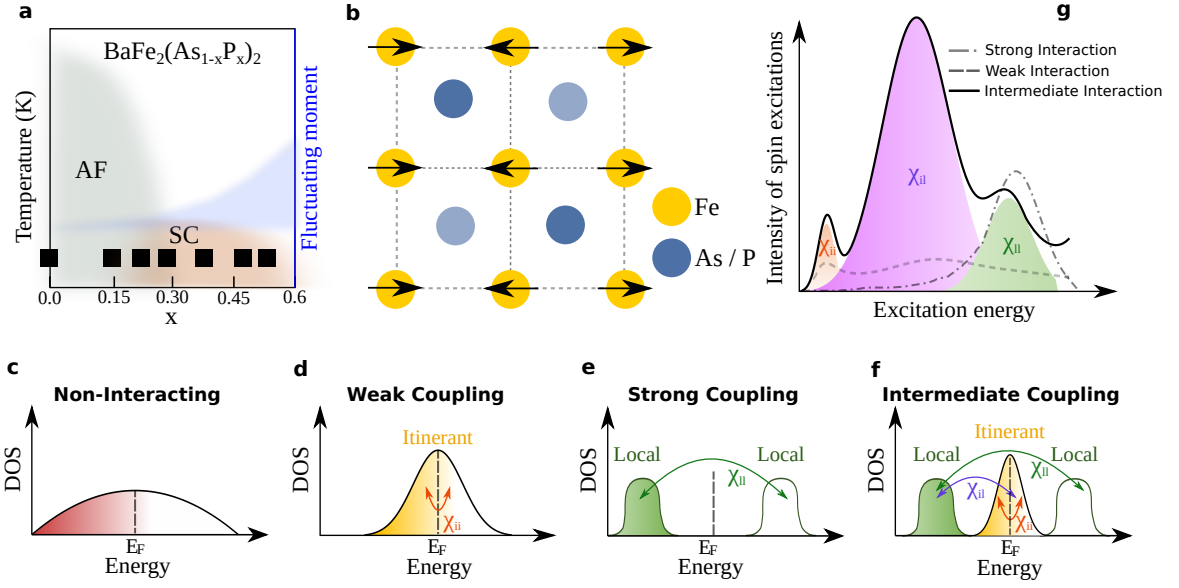


FIG. 1. **Phase diagram, structure, and excitations of $\text{BaFe}_2(\text{As}_{1-x}\text{P}_x)_2$.** **a** Phase diagram of $\text{BaFe}_2(\text{As}_{1-x}\text{P}_x)_2$. The black squares represent the doping levels and temperature measured in our work. As blue line, we schematically depict the expected behaviour of the fluctuating moment. **b** Schematic real space magnetic structure of BaFe_2As_2 . **c-f** Density of states (DOS) as a function of quasiparticle energy. Non-interacting **c**, weak-coupling Random Phase Approximation (RPA) approximation **d**, strong coupling **e**, and intermediate coupling Momentum Resolved Density Fluctuation theory (MRDF) **f**. **g** Excitations spectrum of the spin excitations arising from weak, strong, and intermediate coupling.

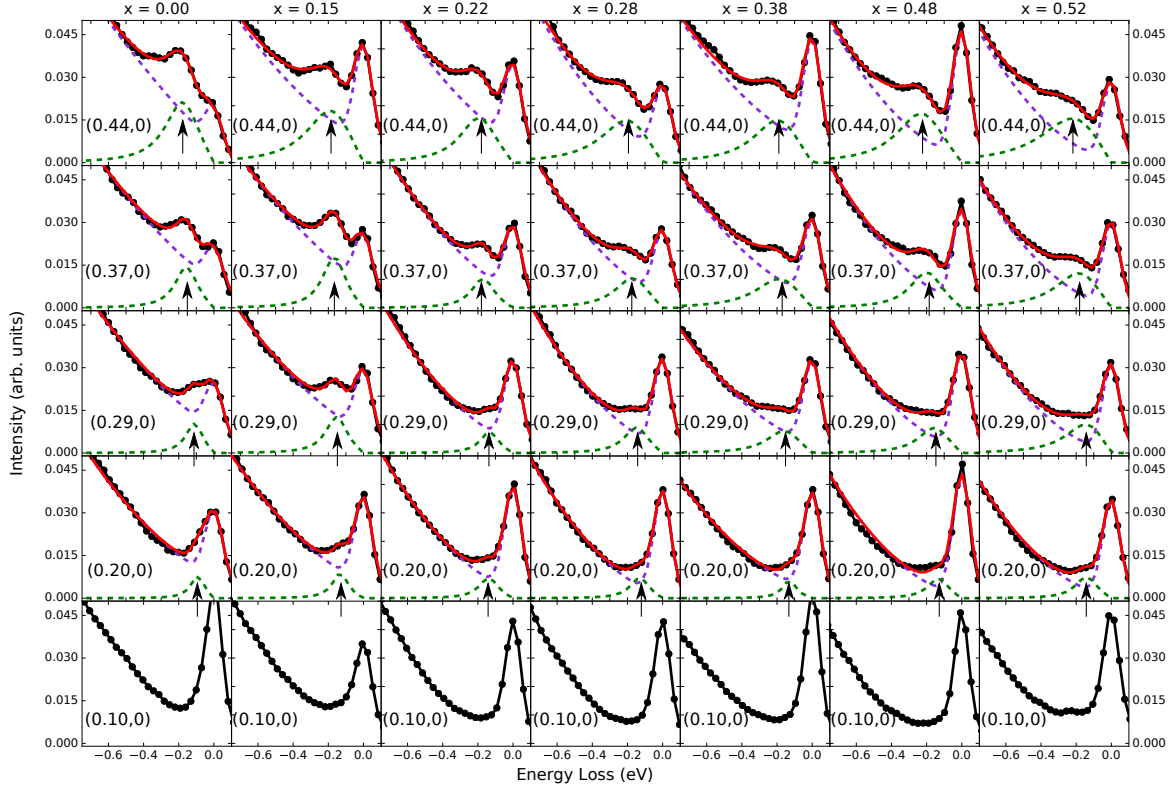


FIG. 2. Resonant Inelastic X-ray Scattering (RIXS) spectra at low energy loss for $\text{BaFe}_2(\text{As}_{1-x}\text{P}_x)_2$ along $(0, 0) \rightarrow (\text{H}, 0)$. Momentum dependence of RIXS spectra along $(0, 0) \rightarrow (0.44, 0)$ for $x = 0.00, 0.15, 0.22, 0.28, 0.38, 0.48,$ and 0.52 . The incoming photons are π polarised and the energy is tuned to the maximum of the Fe L_3 absorption edge. Experimental data are shown as black dots, background, and elastic peak as purple dashed line and magnetic peaks as green dashed line. The sum of background, elastic and magnetic peaks is depicted as red solid line. At low q_{\parallel} a fitting is unreliable, so no fitting was attempted.

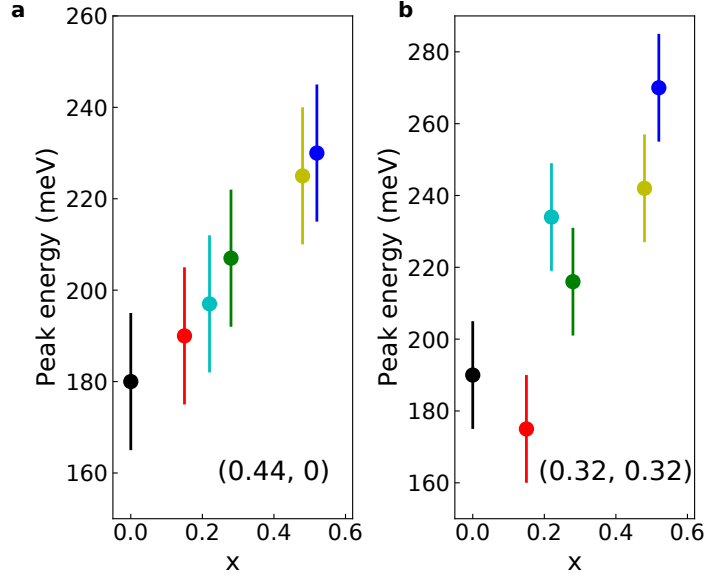


FIG. 3. **Summary of spin excitations.** **a** Dots with error bars: Maximum of the spin excitations' peak detected by Resonant Inelastic X-ray Scattering (RIXS) at (0.44,0). **b** Dots with error bars: Maximum of the spin excitations' peak detected by RIXS at (0.32,0.32). The error bars are defined by the uncertainty of locating the zero energy position in the raw RIXS spectra. We took conservatively 30 meV (1 pixel of our detector) which is much larger than the error resulting from the fitting analysis.

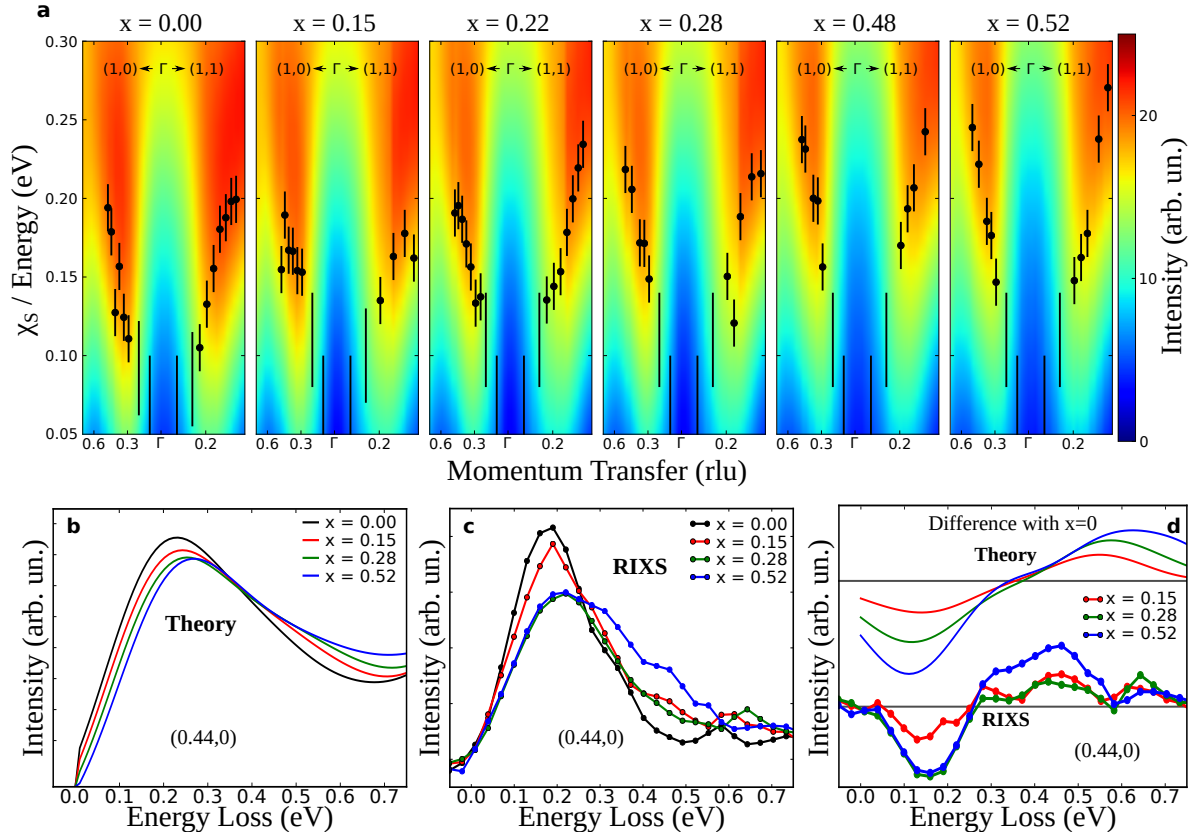


FIG. 4. **Evolution of spin excitations.** **a** Color map: Spin susceptibility (χ_s) calculated by means of Momentum Resolved Density Fluctuations theory (MRDF) self-energy corrected Density Functional Theory (DFT) calculations. Black dots with error bars: Maximum of the spin excitations peak detected by Resonant Inelastic X-ray Scattering (RIXS). The error bars are defined by the uncertainty of locating the zero energy position in the raw RIXS spectra. We took conservatively 30 meV (1 pixel of our detector) which is much larger than the error resulting from the fitting analysis. **b** Evolution of the excitations spectrum with doping in the MRDF framework at $(0.44,0)$. **c** Peak of spin excitations from RIXS for $x = 0.00, 0.15, 0.28, 0.52$ at $(0.44,0)$. **d** Difference of the spin excitations between doped and parent compound of RIXS spectra and MRDF calculations.

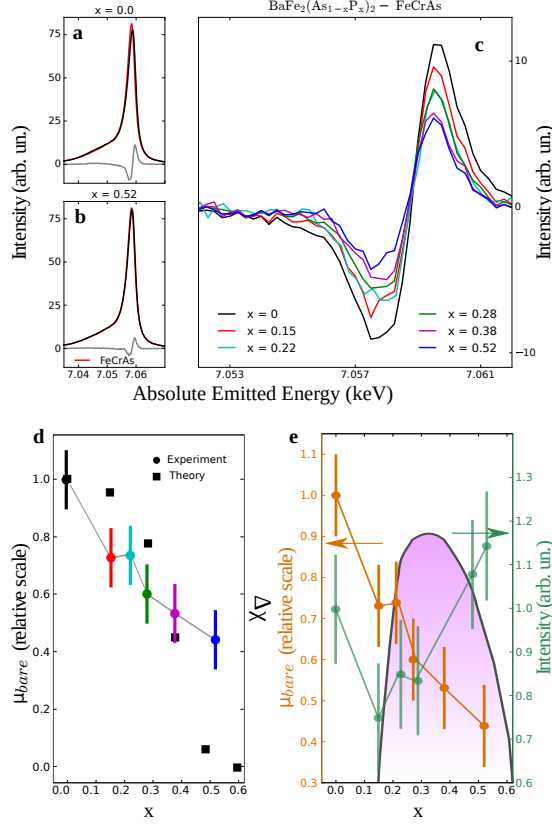


FIG. 5. **Fe-K β X-ray Emission Spectroscopy (XES) and difference spectra for $\text{BaFe}_2(\text{As}_{1-x}\text{P}_x)_2$.** K β XES for $x = 0.00$, and 0.52 (**a,b** as black lines) and reference spectrum of FeCrAs (**a,b** as red lines). The Integrated Area Difference (IAD) is displayed as grey line. **c** Summary of IADs for all the samples. **d** Values of local magnetic moment extracted from XES compared with theoretical estimates of the Fermi surface (FS) nesting strength. The nesting strength is calculated integrating the static susceptibility at the nesting wavevector. The error bars on the values of μ_{bare} are systematic due to the normalization and subtraction steps, thus all the values have an error of ± 0.1 with respect to the values assumed by the parent compound. **e** Summary of local magnetic moment from XES (orange) and intensity of spin excitations (green) integrating the fitting from the Resonant Inelastic X-ray Scattering (RIXS) spectra at high momenta (three highest momenta) along (H,0) and (H,H) as a function of doping across the phase diagram of $\text{BaFe}_2(\text{As}_{1-x}\text{P}_x)_2$. In order to visualize the reciprocal redistribution of local magnetic moments and spin excitations we represent the superconducting dome as a purple shaded area in the background. The error bars on the intensity of the spin excitations have been quantified in ± 0.1 with respect to the value of the parent compound. The fitting error are actually smaller but the sum procedure at different q points produces a propagation of the errors, so we set a slightly higher upper boundary.